Superconductors, orbital magnets and correlated states in magic-angle bilayer graphene

https://doi.org/10.1038/s41586-019-1695-0

Received: 15 March 2019

Accepted: 12 August 2019

Published online: 30 October 2019

Xiaobo Lu[1], Petr Stepanov[1], Wei Yang[1], Ming Xie[2], Mohammed Ali Aamir[1], Ipsita Das[1], Carles Urgell[1], Kenji Watanabe[3], Takashi Taniguchi[3], Guangyu Zhang[4], Adrian Bachtold[1], Allan H. MacDonald[2] & Dmitri K. Efetov[1]*

Superconductivity can occur under conditions approaching broken-symmetry parent states[1]. In bilayer graphene, the twisting of one layer with respect to the other at 'magic' twist angles of around 1 degree leads to the emergence of ultra-flat moiré superlattice minibands. Such bands are a rich and highly tunable source of strong-correlation physics[2–5], notably superconductivity, which emerges close to interaction-induced insulating states[6,7]. Here we report the fabrication of magic-angle twisted bilayer graphene devices with highly uniform twist angles. The reduction in twist-angle disorder reveals the presence of insulating states at all integer occupancies of the fourfold spin–valley degenerate flat conduction and valence bands—that is, at moiré band filling factors $\nu = 0, \pm1, \pm2, \pm3$. At $\nu \approx -2$, superconductivity is observed below critical temperatures of up to 3 kelvin. We also observe three new superconducting domes at much lower temperatures, close to the $\nu = 0$ and $\nu = \pm1$ insulating states. Notably, at $\nu = \pm1$ we find states with non-zero Chern numbers. For $\nu = -1$ the insulating state exhibits a sharp hysteretic resistance enhancement when a perpendicular magnetic field greater than 3.6 tesla is applied, which is consistent with a field-driven phase transition. Our study shows that broken-symmetry states, interaction-driven insulators, orbital magnets, states with non-zero Chern numbers and superconducting domes occur frequently across a wide range of moiré flat band fillings, including close to charge neutrality. This study provides a more detailed view of the phenomenology of magic-angle twisted bilayer graphene, adding to our evolving understanding of its emergent properties.

Interactions dominate over single-particle physics in flat-band electronic systems, and can give rise to insulating states at partial band fillings[3,4], superconductivity[8] and magnetism[9–14]. Recently, correlated insulating phases and strongly coupled superconducting domes have been found in ultra-flat bands of magic-angle twisted bilayer graphene (MAG) close to half-filling ($\nu = \pm2$), establishing graphene as a platform for the investigation of strongly correlated two-dimensional electrons[6,15–18]. MAG has several advantages that should enable new insights into these systems: the correlations can be accurately controlled by varying the twist angle between the two graphene layers; techniques for the fabrication of ultra-clean graphene layers are well-established; and the electron density ($n_0 = A_0^{-1} \approx 10^{12}$ cm^{-2}, where A_0 is the area of the moiré unit cell) that is required to fill a moiré superlattice band can be adequately supplied by electrical gates.

Here we report the observation of correlated states at all integer fillings of $\nu = n/n_0$ (where n is the gate-modulated carrier density), including at charge neutrality, and the occurrence of new superconducting domes and orbital magnetic states in MAG. When interactions are neglected, the two low-energy moiré bands of MAG have fourfold spin–valley flavour degeneracies, which implies that the density measured from the carrier neutrality point (CNP) is $4n_0$ when the flat conduction band is full and $-4n_0$ when the valence band is empty[2,19]. Interactions can lift the flavour degeneracies and give rise to completely empty or full spin–valley polarized flat bands—with interaction-induced gaps at all integer values of ν—in place of the symmetry-protected Dirac points that connect the conduction and valence bands for each flavour[10]. The many-body physics of these bands is highly sensitive to the twist angle θ and the interaction strength ε^{-1} (where ε is the effective dielectric constant in MAG). In some cases—depending on the details of the electronic structure—bands can have non-zero Chern numbers[9,10,20–23], allowing for the possibility of orbital magnetism and anomalous Hall effects.

[1]ICFO – Institut de Ciencies Fotoniques, The Barcelona Institute of Science and Technology, Castelldefels, Barcelona, Spain. [2]Department of Physics, University of Texas at Austin, Austin, TX, USA. [3]National Institute for Materials Science, Tsukuba, Japan. [4]Beijing National Laboratory for Condensed Matter Physics and Institute of Physics, Chinese Academy of Sciences, Beijing, China. *e-mail: dmitri.efetov@icfo.eu

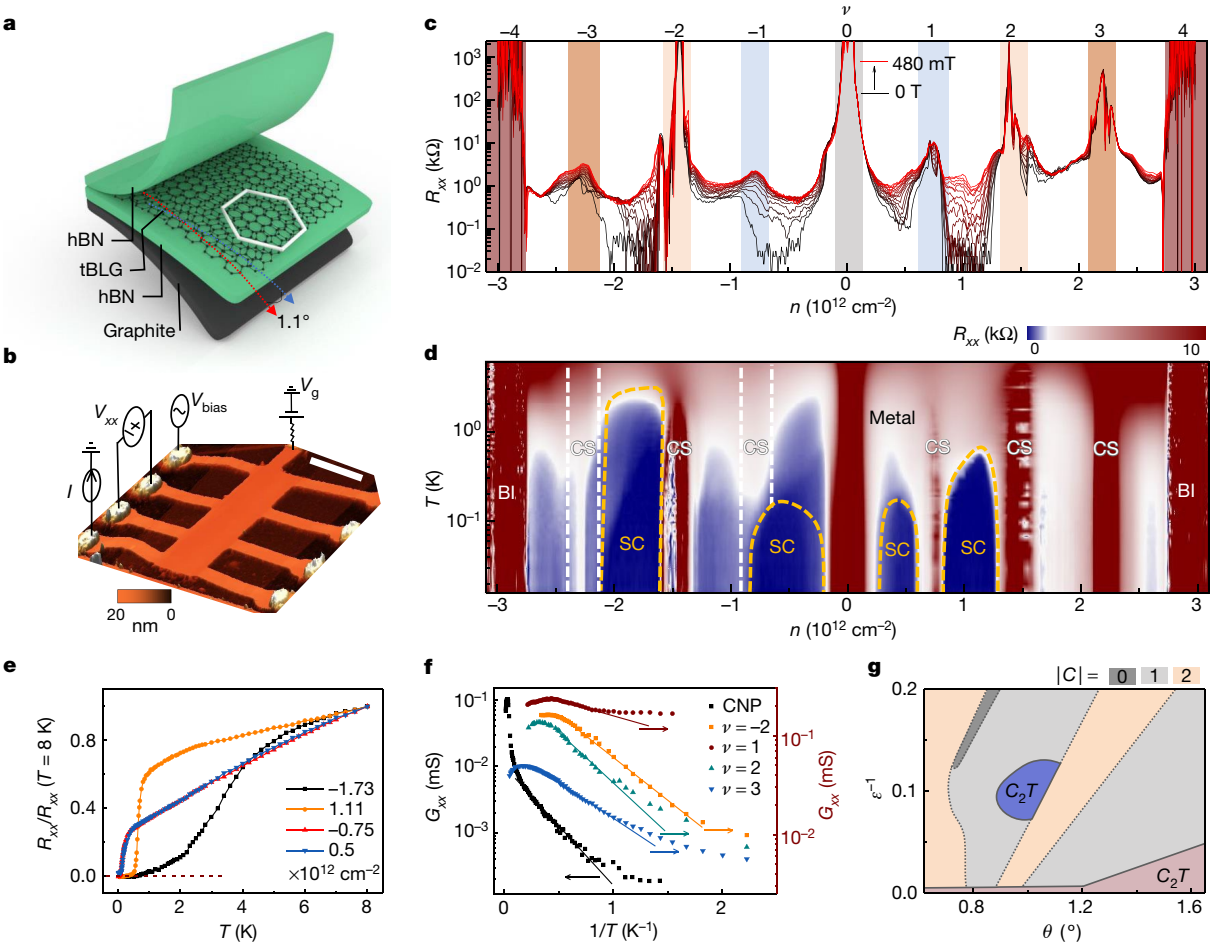

Fig. 1 | Integer-filling correlated states and new superconducting domes. **a**, Schematic of a typical MAG device. **b**, Atomic force microscopy image and schematic of how various measurements are obtained. Scale bar, 2 μm. **c**, Four-terminal longitudinal resistance plotted against carrier density at different perpendicular magnetic fields from 0 T (black trace) to 480 mT (red trace). **d**, Colour plot of longitudinal resistance against carrier density and temperature, showing different phases including metal, band insulator (BI), correlated state (CS) and superconducting state (SC). The boundaries of the superconducting domes—indicated by yellow lines—are defined by 50% resistance values relative to the normal state. Note that the transition from the metal to the superconducting state is not sharp at some carrier densities, which adds uncertainty to the value of T_c extracted. **e**, Longitudinal resistance at optimal doping of the superconducting domes as a function of temperature. The resistance is normalized to its value at 8 K. Note that data points for $n = -7.5 \times 10^{11}$ cm^{-2} are overlaid by the data points for $n = 5 \times 10^{11}$ cm^{-2}, as both curves follow a very similar line. **f**, Conductance G_{xx} plotted against inverse temperature at carrier densities corresponding to $\nu = 0, 1, \pm 2$ and 3. The straight lines are fits to $G_{xx} \propto \exp(-\Delta/2kT)$ (where Δ is the size of the correlation-induced gap and k is the Boltzmann constant), for temperature-activated behaviour, and give gap values of 0.35 meV ($\nu = -2$), 0.14 meV ($\nu = 1$), 0.37 meV ($\nu = 2$), 0.27 meV ($\nu = 3$) and 0.86 meV ($\nu = 0$; CNP). **g**, Mean-field phase diagram for neutral $\nu = 0$ (CNP) twisted bilayer graphene, as a function of twist angle and interaction strength, showing different configurations of C_2T symmetry and Chern number (C). Red and blue regions with solid outlines indicate states that do not break symmetry, and therefore have bands with no Berry curvature and vanishing Chern number. Blue indicates a gapped state and red indicates a gapless state. Zones filled with other colours indicate gapped states that break C_2T symmetry and have bands with different Chern numbers, as shown.

Figure 1a is a schematic of a typical graphite-gated, hexagonal boron nitride (hBN)-encapsulated MAG heterostructure device. The atomic force microscopy image in Fig. 1b shows the high structural homogeneity of the device. Figure 1c shows four-terminal resistance R_{xx} as a function of n at different out-of-plane magnetic fields $B_\perp$, measured at a temperature T of 16 mK. We find strong resistance peaks at $n = 4n_0 \approx \pm 3 \times 10^{12}$ cm^{-2} that mark the edges of the flat bands, consistent with previous studies[3,6,18]. The full-band density corresponds to an average twist angle across the device of about 1.10°. By comparing $2n_0$ values extracted from two-terminal measurements between different contact pairs (Extended Data Fig. 4), we estimate that the variation in twist angle ($\Delta\theta$) is only around 0.02° over a span of about 10 μm. Such homogeneity in the twist angle is, to our knowledge, unprecedented in a MAG device.

In addition to the resistance peaks at the CNP and at $\nu = \pm 4$, we also observe interaction-induced resistance peaks at all non-zero integer fillings of the moiré bands ($\nu = \pm 1, \pm 2, \pm 3$), corresponding to 1, 2 and 3 electrons (+) or holes (−) per moiré unit cell (Fig. 1c). Signatures of some of these resistive states have been observed previously[3,6,18,24], but they are much more strongly developed here. From temperature-dependent transport behaviour over a range of 10 K (Fig. 1f), it is possible to extract the activated gap size of the correlated insulator states. We obtain values of 0.34 meV ($\nu = -2$), 0.37 meV ($\nu = 2$) and 0.25 meV ($\nu = 3$). Evidence for thermally activated transport is much weaker for the $\nu = 1$ state (0.14 meV) and is entirely absent for the $\nu = -3$ and $\nu = -1$ states, which might indicate that these are correlated semi-metallic states rather than insulating states[25].

Our device also shows clear temperature-activated transport behaviour below 33 K at the CNP, with an extracted gap size of 0.86 meV. Gaps at the CNP do not require broken flavour symmetries, but they do require that at least one of the emergent C_3 and C_2T symmetries—which prevent CNP bands from touching—be broken. These symmetries can be explicitly broken by crystallographic alignment of the MAG and hBN

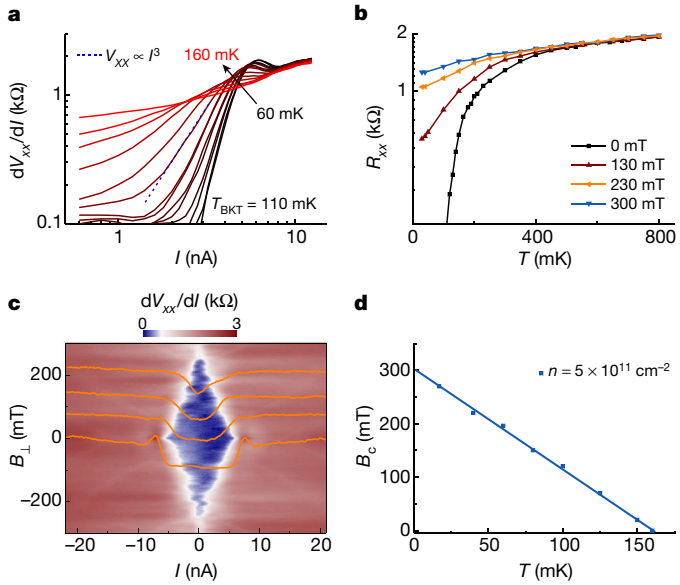

Fig. 2 | The superconducting dome at fillings between $\nu = 0$ and $\nu = 1$. **a**, Differential resistance plotted against d.c. bias current at various temperatures from 60 mK (black trace) to 160 mK (red trace). The blue dashed line is a fit to the $V_{xx} \approx I^3$ power law, and identifies a BKT transition at a temperature (T_{BKT}) of around 110 mK. **b**, Longitudinal resistance plotted against temperature at various out-of-plane magnetic fields, showing that normal levels of resistance are restored at magnetic fields greater than 300 mT. **c**, Two-dimensional colour plot of the differential resistance as a function of magnetic field and excitation current at 16 mK. The orange traces show differential resistance plotted against current at magnetic field values of 225 mT, 150 mT, 75 mT and 0 T (top to bottom). **d**, Values of the critical magnetic field at various temperatures. The straight line is a fit to the Ginzburg–Landau expression. For all measurements in **a**–**d**, the carrier density was fixed at optimal doping of the dome $n = 5 \times 10^{11}$ cm^{-2}.

layers; however, careful inspection of the angle between these (see Supplementary Information) allows us to rule out this scenario. As we also do not observe any other signatures of hBN alignment, such as satellite resistance peaks[9], we conclude that the gap at CNP probably originates as a result of interactions.

The existence of a non-trivial gap at the CNP has strong implications for the properties of other gapped MAG states. Mean-field theory (Fig. 1g, Supplementary Information), predicts gapped states at neutrality over a wide range of twist angles and interaction strengths. Gapped states at non-zero integer values of ν are expected only when the moiré superlattice band width is smaller than the exchange shift produced by band occupation, and this occurs only near the magic angle. Overall our calculations demonstrate that insulating—or for weak interactions, semi-metallic states—are common at all integer values of ν, as observed experimentally. This mean-field phase diagram does not allow for broken translational symmetry, which appears not to be required for our experiments. If broken translational symmetry did have a key role in establishing insulating states, they would be expected at moiré band fillings $\nu = n + p/3$ where p and n are integers; this is not consistent with our experimental observations.

Notably, in four distinct carrier-density intervals between integer filling factors, we observe sharp decreases in the resistance of the device with decreasing temperature (Fig. 1e), which can be restored by the application of a small perpendicular magnetic field $B_\perp < 500$ mT (Fig. 2b). Figure 1d shows a colour plot of resistance against temperature and carrier density, in which four dome-shaped pockets of low resistance flank the most resistive states. In three of these domes, the resistance decreases to zero (Fig. 1e, Extended Data Figs. 5, 7), which is consistent with superconductivity. In the fourth region (at $n = 5 \times 10^{11}$ cm^{-2}) the resistance remains slightly greater than zero, owing to insufficient cooling of electrons below 100 mK in the cryostat[7,18].

In the dome close to $-2n_0$, we observe a superconducting transition. Although this has been reported previously, the superconducting transition temperature T_c (defined as half the normal-state resistance) of 3 K that we observe here is considerably higher than the previous value[6] of around 1.7 K. The other superconducting domes, which to our knowledge are all observed here for the first time, have much lower T_c values and much sharper transitions. We identify a superconducting dome between n_0 and $2n_0$ with $T_c \approx 650$ mK, and two domes between the CNP and $\pm n_0$ with $T_c \approx 160$ mK and $T_c \approx 140$ mK, respectively. As can be seen in Fig. 1d and Extended Data Fig. 6, it is likely that additional superconducting domes are developing between other filling factors; however, these are not fully developed, and are presumably obscured by the inhomogeneity that remains in our improved samples.

Figure 2 shows the signatures of the newly observed superconducting domes (exemplified by the state between CNP and n_0; all other states are described in detail in Extended Data Fig. 7 and Extended Data Table 1). In Fig. 2a, the differential resistance dV_{xx}/dI is plotted against the d.c. bias current I at various temperatures. At 60 mK, the traces display the nonlinear resistance typical of two-dimensional superconductivity, with a sharp resistive transition for $I > I_c \approx 3$ nA (where I_c is the critical supercurrent). The blue dashed line is a power-law fit to $dV_{xx}/dI \approx I^2$, consistent with two-dimensional superconductivity described by the Berezinskii–Kosterlitz–Thouless (BKT) theory, showing a transition temperature T_{BKT} of around 110 mK.

The temperature dependence of the resistance R_{xx} at various magnetic fields is illustrated in Fig. 2b. The superconductivity signal is gradually weakened upon increasing the applied field, and R_{xx} varies almost linearly with temperature above a critical field $B_c \approx 300$ mT. The suppression of superconductivity by the magnetic field is further exemplified by Fig. 2c, which shows a plot of the differential resistance as a function of the magnetic field and the excitation current I at 16 mK. The critical supercurrent I_c is reduced by application of a magnetic field, reaching zero when $B_c > 300$ mT. From these measurements, we extract the temperature-dependent critical magnetic field B_c (defined by 50% of the normal state R_{xx} value). By fitting to the expression from Ginzburg–Landau theory, $B_c = [\Phi_0/(2\pi\xi^2)](1 - T/T_c)$, we extract a coherence length $\xi_{GL(T=0\,K)}$ of around 32 nm. Here $\Phi_0 = h/(2e)$ is the superconducting flux quantum, h is Planck's constant and e is the electron charge.

We have studied the response of the flat bands to an applied magnetic field at a temperature of 100 mK. Figure 3a shows a colour map of the resistance as a function of carrier density and magnetic field, and the corresponding schematic highlights the trajectories of the resistance maxima. We find sets of Landau fans that originate from the CNP and from most of the resistive states with an integer filling factor. In previous studies, Landau levels were identified only on the high-carrier-density sides of insulating states[3,18]. Here, we also observe Landau levels dispersing to lower densities. The vanishing carrier densities near most integer filling factors—as evidenced by both Landau fans and weak field Hall resistivities (Extended Data Fig. 3)—suggest that the fourfold spin–valley band degeneracy of the non-interacting state is lifted over a large range of filling factors, resetting the carrier density per band.

Our observations suggest that a rich variety of spin–valley broken-symmetry states occur as a function of carrier density and magnetic field. Landau levels that can be traced to the CNP exhibit fourfold degeneracy with a filling-factor sequence of $\nu_L = \pm 4, \pm 8, \pm 12, \ldots$, as well as spin–valley broken-symmetry states with $\nu_L = \pm 2$. The Landau levels that fan out from $\nu = 2(-2)$ follow a sequence of $\nu_L = 2(-2), 4(-4), 6(-6), \ldots$ at low magnetic field, indicating partially lifted degeneracy for either spin or valley. Quantum oscillations from $\nu = -2$ exhibit a dominant degeneracy sequence of $\nu_L = -3, -5, -7, \ldots$ at high magnetic field. Near $\nu = -3$, quantum oscillations exhibit fully lifted degeneracy of Landau levels with filling factors $\nu_L = -1, -2, -3, -4, \ldots$. The Landau fans that emerge from insulating

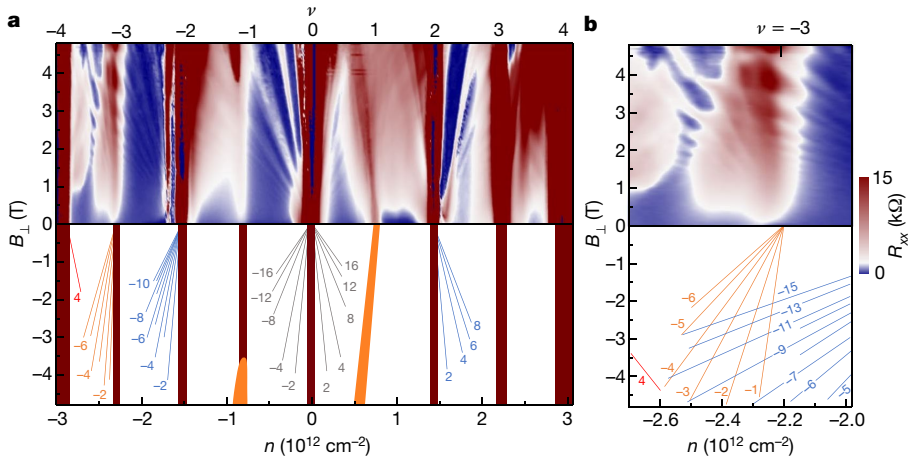

Fig. 3 | Shubnikov–de Haas oscillations in the MAG flat bands. a, Top, colour map of longitudinal resistance plotted against carrier density and magnetic field. Bottom, the corresponding schematic that identifies visible Landau level fans with a dominant degeneracy. The Landau fan diagram diverging from the CNP ($\nu = 0$) follows a fourfold degenerate sequence with $\nu_L = \pm 4, \pm 8, \pm 12, \ldots$, with symmetry-broken states at $\nu_L = \pm 2$. The fans from $\nu = 2(-2)$ follow a twofold degenerate $\nu_L = -2(2), -4(4), -6(6), \ldots$ sequence, with broken-symmetry states at $\nu_L = -3, -5, -7, \ldots$. The $\nu = -3$ fan follows a single degenerate $\nu_L = -1, -2, -3, -4, \ldots$ sequence. Emergent correlated phases at all integer moiré fillings, including the CNP ($\nu = 0$), are highlighted in dark red. Chern insulating states are highlighted in orange. **b**, Magnification of **a** around the $\nu = -3$ state, showing signatures similar to a Hofstadter butterfly spectrum with criss-crossing Landau levels fanning out from $\nu = -3$ and $\nu = -2$ filling states.

states all extrapolate to a carrier density that vanishes at integer moiré band filling factors.

We also find that the degeneracies of Landau levels originating from the CNP and $\nu = -2$ change when crossing the $\nu = -1$ and $\nu = -3$ states, suggestive of first-order phase transitions that change band degeneracies. In particular, as is shown in Fig. 3b, Landau levels from the $\nu = -2$ and $\nu = -3$ states display a criss-crossing pattern—superficially similar to that of a Hofstadter butterfly, but distinct in that the Landau level indices that can be traced to the $\nu = -3$ state are spaced by one filling, whereas those that can be traced to the $\nu = -2$ state are spaced by two fillings.

It is noteworthy that neither of the $\nu = \pm 1$ correlated states show clear formation of Landau levels. The positions of their resistance maxima do, however, exhibit clear dependencies on the magnetic field and the carrier density. At $\nu = -1$ the resistance state has no slope (dn/dB) at low field; however, above a critical field $B_T \approx 3.6$ T, we observe the sudden development of a slope that is consistent with a Chern number of 1. Furthermore, at $\nu = 1$ the position of the resistance peak shifts to lower carrier density, with a slope that is consistent with a Chern number of 2. The slope of dn/dB in the absence of a Landau-level fan in the $\nu = \pm 1$ correlated states is consistent with Chern insulating states from spin and valley symmetry breaking at odd values of ν. As discussed earlier

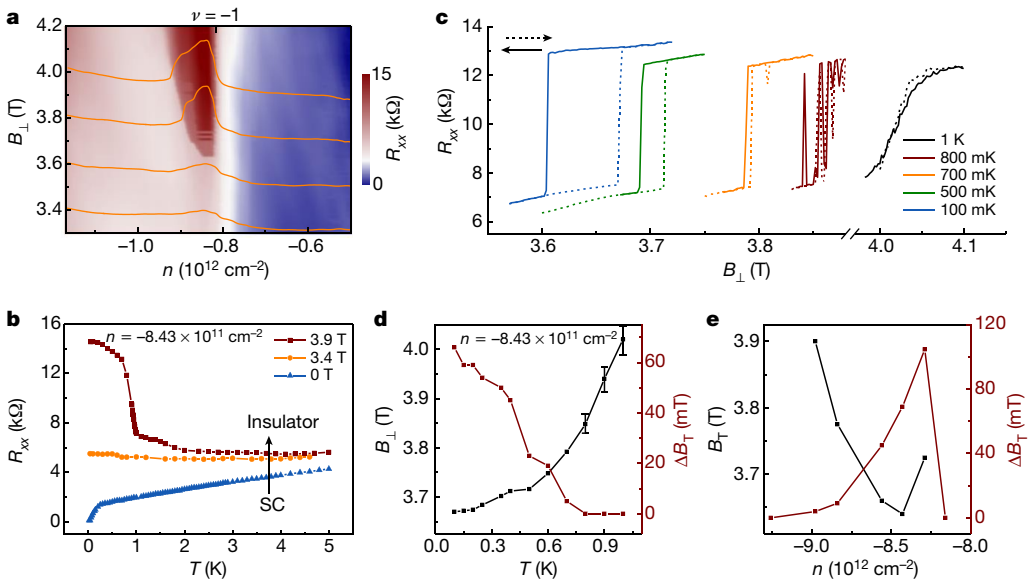

Fig. 4 | Field-driven phase transition near the $\nu = -1$ state. a, Longitudinal resistance plotted as a function of carrier density and out-of-plane magnetic field measured at 16 mK. The orange traces show longitudinal resistance plotted against carrier density with the magnetic field (from top to bottom) fixed at 4 T, 3.8 T, 3.6 T and 3.4 T. **b**, Longitudinal resistance plotted against temperature at various magnetic fields. **c**, Longitudinal resistance plotted against magnetic field at various temperatures, with dashed and solid lines corresponding to increasing and decreasing magnetic field, respectively. **d**, Dependence of the critical magnetic field (extracted from up sweeps) and the hysteresis value on temperature. Note that the transition above 800 mK is not sharp, adding uncertainty to the extracted critical field values. In **b**–**d**, the carrier density is fixed at -8.43×10^{11} cm^{2}. **e**, Dependence of the critical magnetic field and the hysteresis value on the carrier density at 100 mK.

and as predicted by mean-field theory, valley-projected bands in insulating states can have non-zero Chern numbers that compete closely with states with zero Chern numbers. Although we cannot resolve quantized values in R_{xy} nor zero resistance in R_{xx}, as expected for a Chern insulating state, we do not do so for the other Landau levels in Fig. 3a either. We therefore conclude that our devices are still too inhomogeneous to observe quantization over the entire device.

Exactly at the transition at which the slope of the $\nu = -1$ resistive state in Fig. 3a changes from $dn/dB = 0$ to a dn/dB consistent with Chern number 1, we find a strong hysteretic increase of R_{xx} and R_{xy}; this is indicative of a possible magnetic-field-induced first-order phase transition. Figure 4a displays a plot of R_{xx} as a function of n and $B_\perp$. Figure 4b displays the temperature-dependent resistance $R_{xx}(T)$ near $\nu = -1$ (or $n = -8.43 \times 10^{11}\ \mathrm{cm}^{-2}$) for a series of magnetic field values. Whereas at $B_\perp = 0$ T, $R_{xx}(T)$ shows a typical metal-superconductor phase transition, above $B_\perp > 3.6$ T and below $T < 0.9$ K, $R_{xx}(T)$ has a sharp jump and an insulating temperature dependence.

Figure 4c shows plots of R_{xx} against the magnetic field at $\nu = -1$ for up and down sweeps of the magnetic field. Below 800 mK, the curves show sharp jumps in resistance at associated critical transition fields B_T, and demonstrate strong hysteretic behaviour that is dependent on the sweeping direction of the magnetic field; the width of the magnetic field of the hysteresis loop is denoted by ΔB_T. The critical field B_T is always higher for up sweeps than for down sweeps.

Both B_T and ΔB_T are highly temperature-dependent, with B_T shifting to higher values and ΔB_T becoming smaller as the temperature increases. At $T > 800$ mK, the hysteresis almost disappears and the transition becomes broader. The temperature dependencies of B_T and ΔB_T were extracted and are shown in Fig. 4d. The phase transition and hysteresis occur over a narrow range of carrier densities from around $-8.3 \times 10^{11}\ \mathrm{cm}^{-2}$ to $-9 \times 10^{11}\ \mathrm{cm}^{-2}$ (Extended Data Fig. 8b, c) with B_T and ΔB_T at different carrier densities shown in Fig. 4e. Overall, we observe similar behaviour in Hall resistance measurements (Extended Data Fig. 8d). These observations indicate that the origin of the change in the slope dn/dB of the resistance maximum is a first-order phase transition, and is probably due to a competition between correlated states with zero and non-zero Chern numbers at high magnetic fields[26], suggesting the emergence of a field-stabilized orbital magnetic state.

Notably, we have observed superconducting domes close to charge neutrality. To our knowledge, these states represent the lowest carrier density ($n \approx 3 \times 10^{11}\ \mathrm{cm}^{-2}$; counting from CNP) at which superconductivity has been observed. The existence of superconducting domes across a wide range of moiré band fillings must have important implications for our understanding of their origin. Because the density of states diminishes close to the CNP, the appearance of superconductivity seems not to be simply related to a high density of states of the non-interacting bands. Superconductivity occurs adjacent to insulating states that seem—on the basis of Landau fan patterns—to break spin–valley degeneracy, and adjacent to insulating states that do not. Nevertheless, its consistent association with nearby correlated insulator states suggests an exotic pairing mechanism. Conversely, at this point our observation cannot rule out the possibility of conventional electron–phonon coupling superconductivity in metallic states with quasiparticles that evolve adiabatically from those of the non-interacting system and compete with a rich variety of distinct insulating states from which they are separated by first-order phase transition lines[24,27,28]. In this case, it is possible that the consistent high density of states over a broad range of filling factors helps to support superconductivity in the metallic state.

Online content

Any methods, additional references, Nature Research reporting summaries, source data, extended data, supplementary information, acknowledgements, peer review information; details of author contributions and competing interests; and statements of data and code availability are available at https://doi.org/10.1038/s41586-019-1695-0.

1. Lee, P. A., Nagaosa, N. & Wen, X.-G. Doping a Mott insulator: physics of high-temperature superconductivity. *Rev. Mod. Phys*. **78**, 17 (2006).
2. Bistritzer, R. & MacDonald, A. H. Moire bands in twisted double-layer graphene. *Proc. Natl Acad. Sci. USA* **108**, 12233–12237 (2011).
3. Cao, Y. et al. Correlated insulator behaviour at half-filling in magic-angle graphene superlattices. *Nature* **556**, 80–84 (2018).
4. Chen, G. et al. Evidence of a gate-tunable Mott insulator in a trilayer graphene moiré superlattice. *Nat. Phys*. **15**, 237–241 (2019).
5. Tarnopolsky, G., Kruchkov, A. J. & Vishwanath, A. Origin of magic angles in twisted bilayer graphene. *Phys. Rev. Lett*. **122**, 106405 (2019).
6. Cao, Y. et al. Unconventional superconductivity in magic-angle graphene superlattices. *Nature* **556**, 43–50 (2018).
7. Chen, G. et al. Signatures of gate-tunable superconductivity in trilayer graphene moiré superlattice. *Nature* **572**, 215–219 (2019).
8. Kopnin, N., Heikkilä, T. & Volovik, G. High-temperature surface superconductivity in topological flat-band systems. *Phys. Rev. B* **83**, 220503 (2011).
9. Sharpe, A. L. et al. Emergent ferromagnetism near three-quarters filling in twisted bilayer graphene. *Science* **365**, 605–608 (2018).
10. Xie, M. & MacDonald, A. H. On the nature of the correlated insulator states in twisted bilayer graphene. Preprint at https://arxiv.org/abs/1812.04213 (2018).
11. Ochi, M., Koshino, M. & Kuroki, K. Possible correlated insulating states in magic-angle twisted bilayer graphene under strongly competing interactions. *Phys. Rev. B* **98**, 081102 (2018).
12. Dodaro, J. F., Kivelson, S. A., Schattner, Y., Sun, X.-Q. & Wang, C. Phases of a phenomenological model of twisted bilayer graphene. *Phys. Rev. B* **98**, 075154 (2018).
13. Thomson, A., Chatterjee, S., Sachdev, S. & Scheurer, M. S. Triangular antiferromagnetism on the honeycomb lattice of twisted bilayer graphene. *Phys. Rev. B* **98**, 075109 (2018).
14. Nandkishore, R., Levitov, L. & Chubukov, A. Chiral superconductivity from repulsive interactions in doped graphene. *Nat. Phys*. **8**, 158 (2012).
15. Cao, Y. et al. Strange metal in magic-angle graphene with near Planckian dissipation. Preprint at https://arxiv.org/abs/1901.03710 (2019).
16. Po, H. C., Zou, L., Senthil, T. & Vishwanath, A. Faithful tight-binding models and fragile topology of magic-angle bilayer graphene. *Phys. Rev. B* **99**, 195455 (2019).
17. Kim, K. et al. Tunable moiré bands and strong correlations in small-twist-angle bilayer graphene. *Proc. Natl Acad. Sci. USA* **114**, 3364–3369 (2017).
18. Yankowitz, M. et al. Tuning superconductivity in twisted bilayer graphene. *Science* **363**, 1059–1064 (2019).
19. Cao, Y. et al. Superlattice-induced insulating states and valley-protected orbits in twisted bilayer graphene. *Phys. Rev. Lett*. **117**, 116804 (2016).
20. Lian, B., Xie, F. & Bernevig, B. A. The Landau level of fragile topology. Preprint at https://arxiv.org/abs/1811.11786 (2018).
21. Song, Z. et al. All magic angles in twisted bilayer graphene are topological. *Phys. Rev. Lett*. **123**, 036401 (2019).
22. Bultinck, N., Chatterjee, S. & Zaletel, M. P. Anomalous Hall ferromagnetism in twisted bilayer graphene. Preprint at https://arxiv.org/abs/1901.08110 (2019).
23. Zhang, Y.-H., Mao, D. & Senthil, T. Twisted bilayer graphene aligned with hexagonal boron nitride: anomalous Hall effect and a lattice model. Preprint at https://arxiv.org/abs/1901.08209 (2019).
24. Polshyn, H. et al. Phonon scattering dominated electron transport in twisted bilayer graphene. Preprint at https://arxiv.org/abs/1902.00763 (2019).
25. Kondo, T. et al. Quadratic Fermi node in a 3D strongly correlated semimetal. *Nat. Commun*. **6**, 10042 (2015).
26. Kagawa, F., Itou, T., Miyagawa, K. & Kanoda, K. Magnetic-field-induced Mott transition in a quasi-two-dimensional organic conductor. *Phys. Rev. Lett*. **93**, 127001 (2004).
27. Lian, B., Wang, Z. & Bernevig, B. A. Twisted bilayer graphene: a phonon driven superconductor. *Phys. Rev. Lett*. **122**, 257002 (2019).
28. Wu, F., Hwang, E. & Sarma, S. D. Phonon-induced giant linear-in-*T* resistivity in magic angle twisted bilayer graphene: ordinary strangeness and exotic superconductivity. *Phys. Rev. B* **99**, 165112 (2019).

Methods

Device fabrication

Extended Data Fig. 1 displays a step-by-step stacking process for the fabrication of twisted bilayer graphene (tBLG) with a graphite bottom gate. The hBN/tBLG/hBN/graphite stacks were exfoliated and assembled using a van der Waals assembly technique. Monolayer graphene, thin graphite and hBN flakes (around 10-nm thick) were first exfoliated on SiO_2 (around 300 nm)/Si substrate, followed by the 'tear and stack' technique[29] with a polycarbonate (PC)/polydimethylsiloxane (PDMS) stamp to obtain the final hBN/tBLG/hBN/graphite stack. The separated graphene pieces were rotated manually by a twist angle of around 1.2–1.3°. We purposefully chose a larger twist angle during the assembly of the heterostructure owing to the high risk of relaxation of the twist angle to random lower values. To increase the structural homogeneity, we further carried out a mechanical cleaning process to squeeze the trapped blister out and release the local strain[30] (Extended Data Fig. 2). To avoid the uncertainty induced by thermal expansion of the transfer stage, all the stacking process were carried out at a fixed temperature of 100 °C, except that the final stacks were released at 180 °C (the melting point of polycarbonate). We did not perform subsequent high-temperature annealing to avoid relaxation of the twist angle. We further patterned the stacks with PMMA resist and $CHF_3 + O_2$ plasma and exposed the edges of graphene, which was subsequently contacted by Cr/Au (5/50 nm) metal leads using electron-beam evaporation (Cr) and thermal evaporation (Au).

Measurement

Transport measurements were carried out in a dilution refrigerator with a base temperature of 16 mK and a perpendicular magnetic field of up to 5 T. The dilution refrigerator was well filtered to avoid heating of the electrons in our devices. We use superconducting-type coaxial cables (around 2 m long; Lakeshore) from the room-temperature plate to the mixing chamber plate of the cryostat. We add on each line a pi filter (RS 239-191) at room temperature, and a powder filter (Leiden Cryogenics) as well as a two-stage resistor–capacitor filter on a printed circuit board ($R = 1\,\mathrm{k\Omega}$, $C = 100$ nF) at the mixing chamber plate. The total resistance of each line is about 2 kΩ. The sample is located in a copper box with coaxial feedthroughs.

Standard low-frequency lock-in techniques were used to measure the resistance R_{xx} and R_{xy} with an excitation current of about 1 nA at a frequency of 19.111 Hz. In the measurement of differential resistance $\mathrm{d}V/\mathrm{d}I$, an a.c. excitation current (around 0.5 nA) was applied through an a.c. signal (0.5 V) generated by the lock-in amplifier in combination with a 1/100 divider and a 10-MΩ resistor. Before combining with the excitation, the applied d.c. signal passed through a 1/100 divider and a 1-MΩ resistor. As-induced differential voltage was further measured at the same frequency of 19.111 Hz with standard lock-in technique. For measurements in strong magnetic fields we found that the increased contact resistance made it difficult to obtain accurate values of the device resistance. To resolve this issue, we applied a global gate voltage (+20 V) through Si/SiO_2 (around 300 nm) to tune the charge carrier density separately in the device leads.

Twist angle extraction

The total carrier density n tuned by gate is calibrated by Hall measurements at low field (Extended Data Fig. 3). Near charge neutrality and band insulating states, Hall charge carrier density ($n_H = -B/(eR_{xy})$) should closely follow gate-induced carrier density n; that is, $\mathrm{d}n_H/\mathrm{d}n = 1$, providing accurate measurements of the carrier density n.

For different integer (ν) moiré filling states, the total carrier density can be described by $\nu n_0 = \nu A_0^{-1} = 4\nu(1-\cos\theta)/\sqrt{3}\,a^2$, where A_0 is the unit cell area of the periodic moiré pattern, θ is the twist angle and $a = 0.246$ nm is the lattice constant of graphene. The local twist angles between different contacts are extracted with the carrier densities of $\nu = 2$ states shown in Extended Data Fig. 4. The carrier density difference between CNP and $\nu = 2$ states in device D1 ranges from $1.38 \times 10^{12}\ \mathrm{cm}^{-2}$ to $1.45 \times 10^{12}\ \mathrm{cm}^{-2}$, corresponding to local twist angles ranging from 1.09° to 1.12°. For device D2, the local twist angles range from 1.08° to 1.10°.

Data availability

The data that support the findings of this study are available from the corresponding author upon reasonable request.

29. Kim, K. et al. van der Waals heterostructures with high accuracy rotational alignment. *Nano Lett*. **16**, 1989–1995 (2016).
30. Purdie, D. G. et al. Cleaning interfaces in layered materials heterostructures. *Nat. Commun*. **9**, 5387 (2018).

Acknowledgements We are grateful for discussions with P. Jarillo-Herrero, A. Bernevig, M. Yankowitz, A. Young, C. Dean, L. Levitov, A. Vishwanath, M. Fisher, M. Allan and F. Koppens. D.K.E. acknowledges support from the Ministry of Economy and Competitiveness of Spain through the 'Severo Ochoa' program for Centres of Excellence in R&D (SE5-0522), Fundació Privada Cellex, Fundació Privada Mir-Puig, the Generalitat de Catalunya through the CERCA program, the H2020 Programme under grant agreement number 820378, Project: 2D·SIPC and the La Caixa Foundation. A.H.M. and M.X. acknowledge support from Department of Energy grant DE-FG02-02ER45958 and Welch Foundation grant TBF1473. A.B. acknowledges support from the Plan Nacional (RTI2018-097953-B-I00) of MICINN. G.Z. acknowledges support from the National Science Foundation of China under grant numbers 11834017 and 61888102, and the Strategic Priority Research Program of the Chinese Academy of Sciences under grant number XDB30000000.

Author contributions D.K.E. and X.L. conceived and designed the experiments; X.L., W.Y. and P.S. performed the experiments; X.L. and D.K.E. analysed the data; M.X. and A.H.M. performed the theoretical modelling of the data; T.T. and K.W. contributed materials; D.K.E., A.B., M.A.A., I.D., C.U. and G.Z. supported the experiments; X.L., D.K.E., P.S., X.M. and A.H.M. wrote the paper.

Competing interests The authors declare no competing interests.

Additional information

Supplementary information is available for this paper at https://doi.org/10.1038/s41586-019-1695-0.

Correspondence and requests for materials should be addressed to D.K.E.

Peer review information *Nature* thanks David Goldhaber-Gordon and the other, anonymous, reviewer(s) for their contribution to the peer review of this work.

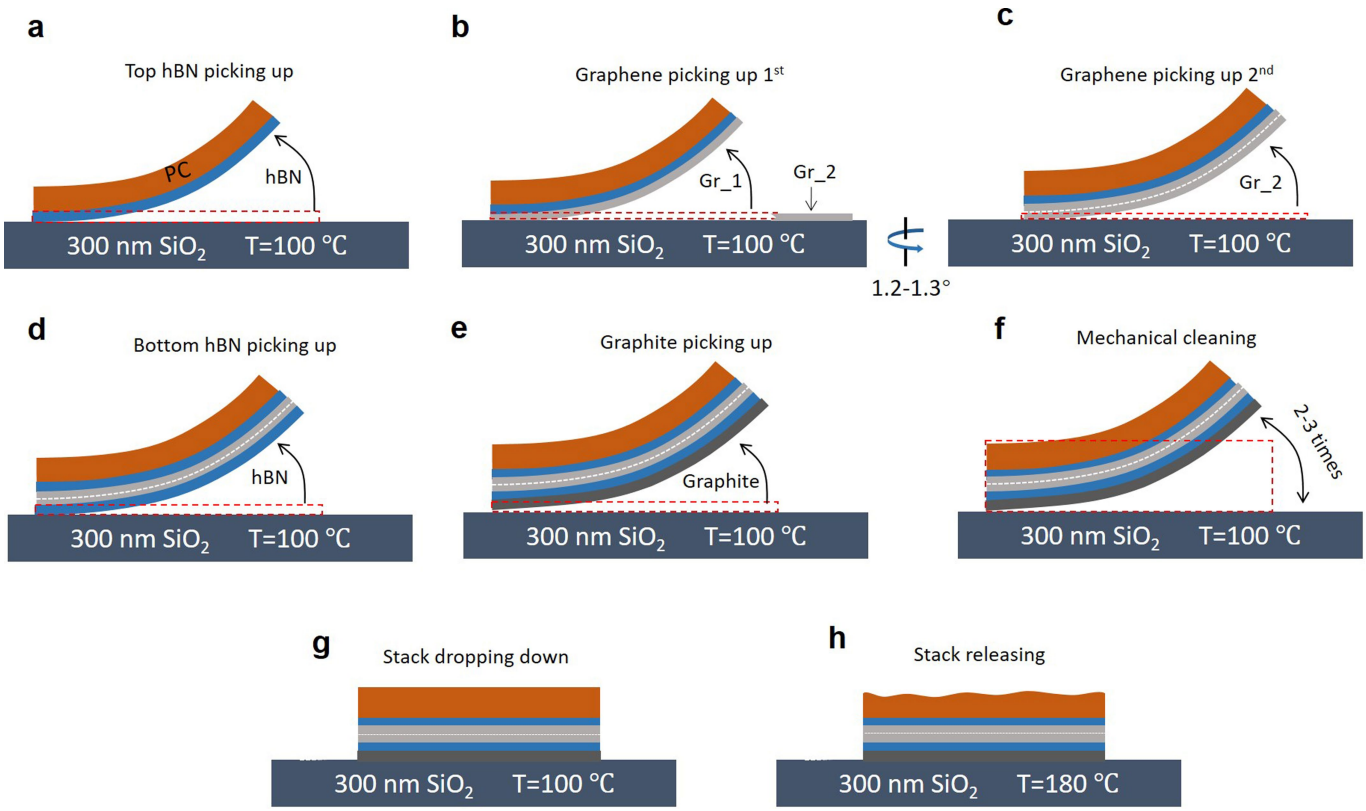

Extended Data Fig. 1 | Schematic of the stacking process for the fabrication of twisted bilayer graphene with graphite bottom gate. a–h, Sequential device fabrication method, describing the tear-and-stack co-lamination process used to create the hBN/tBLG/hBN/graphite stacks.

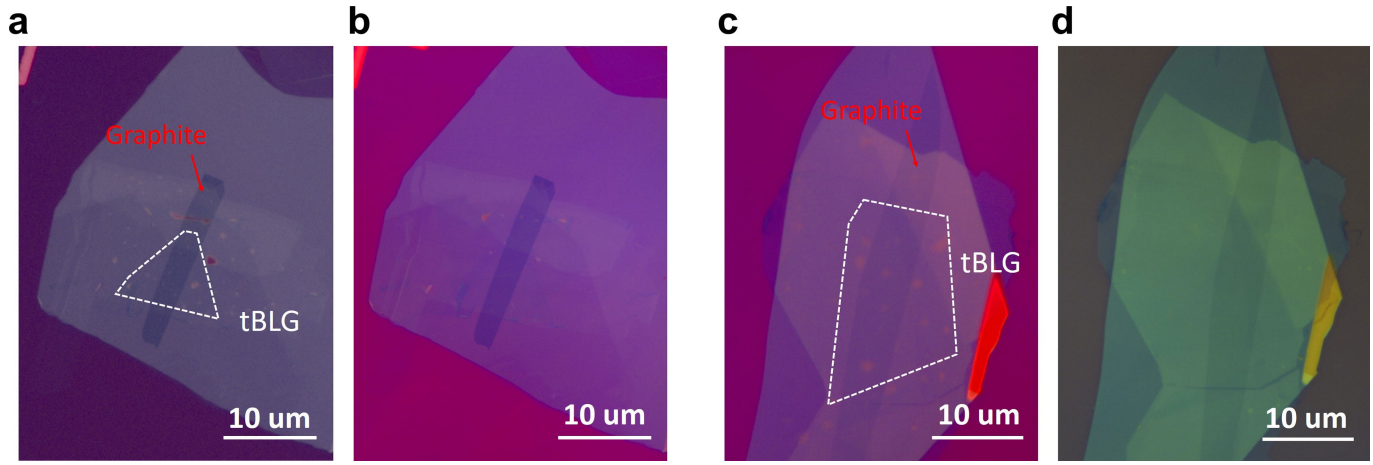

Extended Data Fig. 2 | Mechanical cleaning of twisted bilayer graphene. a–**d**, Optical images of the final stacks before mechanical cleaning (**a**, **c**) and after mechanical cleaning (**b**, **d**).

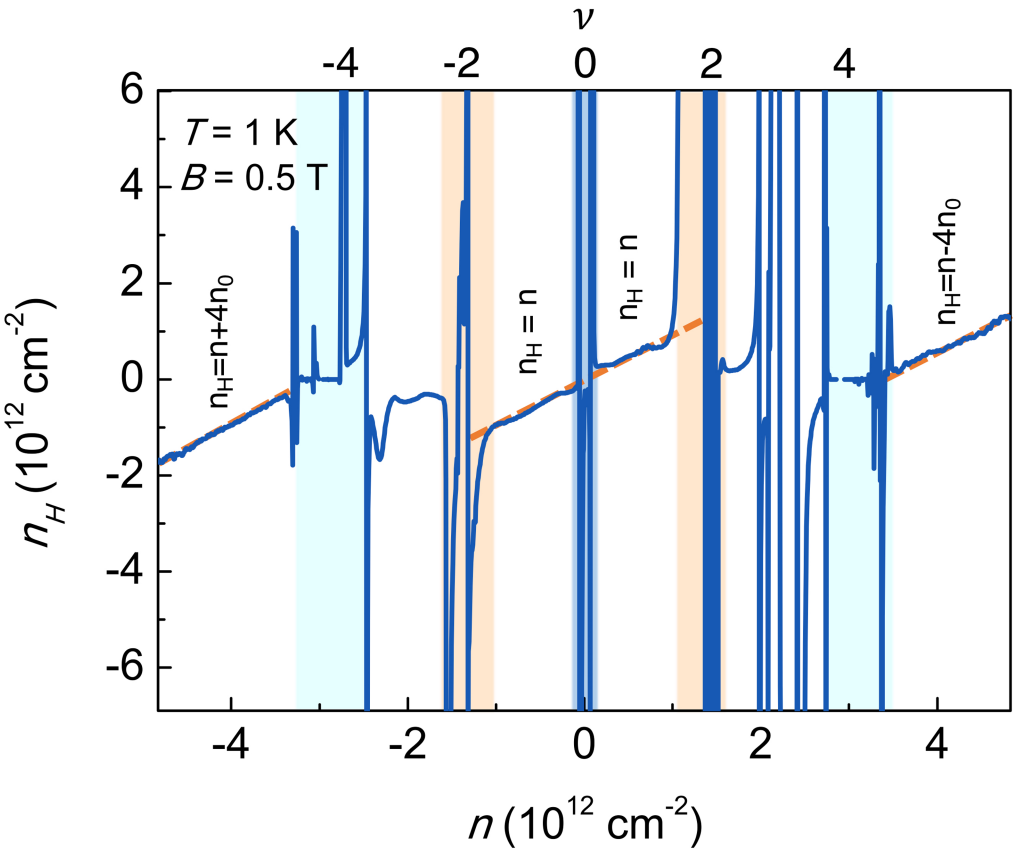

Extended Data Fig. 3 | Hall measurements of device D1. Coloured vertical bars correspond to filling factors $\nu = -4, -2, 2$ and 4. Hall charge carrier density ($n_H = -B/(eR_{xy})$) closely follows the gate-induced carrier density n. Near charge neutrality, $n_H = n$. Beyond the band insulator regions ($\nu = \pm 4$), the Hall density strictly follows $n_H = n \pm 4n_0$.

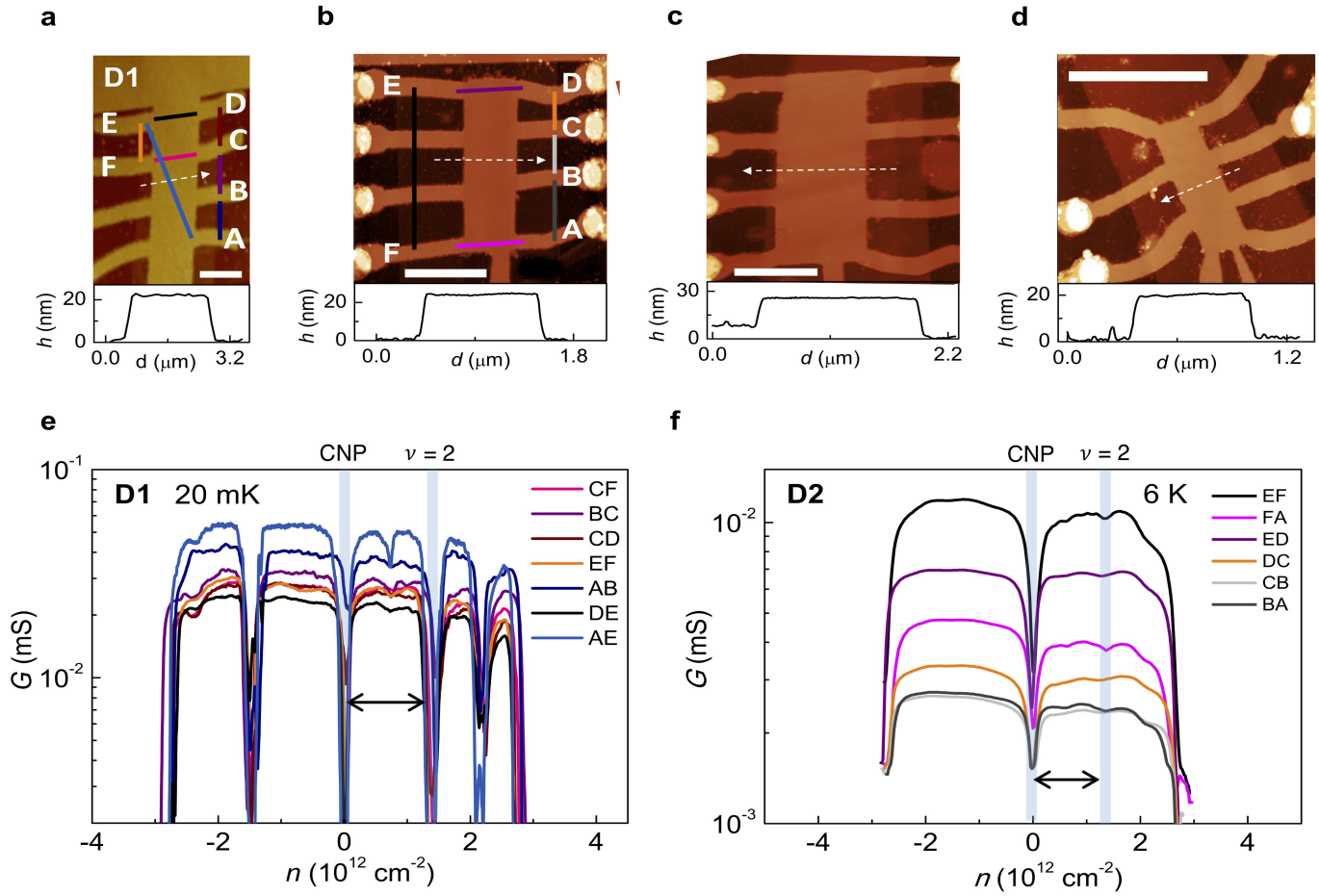

Extended Data Fig. 4 | Measuring the homogeneity of the twist angle. **a**–**d**, Atomic force microscopy images of a set of twisted bilayer graphene samples. Scale bar, 2 μm. Dashed-line arrows correspond to the height profiles shown below the topographies. **e**, **f**, Two-terminal conductance measurements taken between contacts shown in **a** and **b**. Colours correspond to the bars shown in **a** and **b**, respectively. The difference in carrier density between the CNP and the $\nu = 2$ state is used to extract the local twist angle.

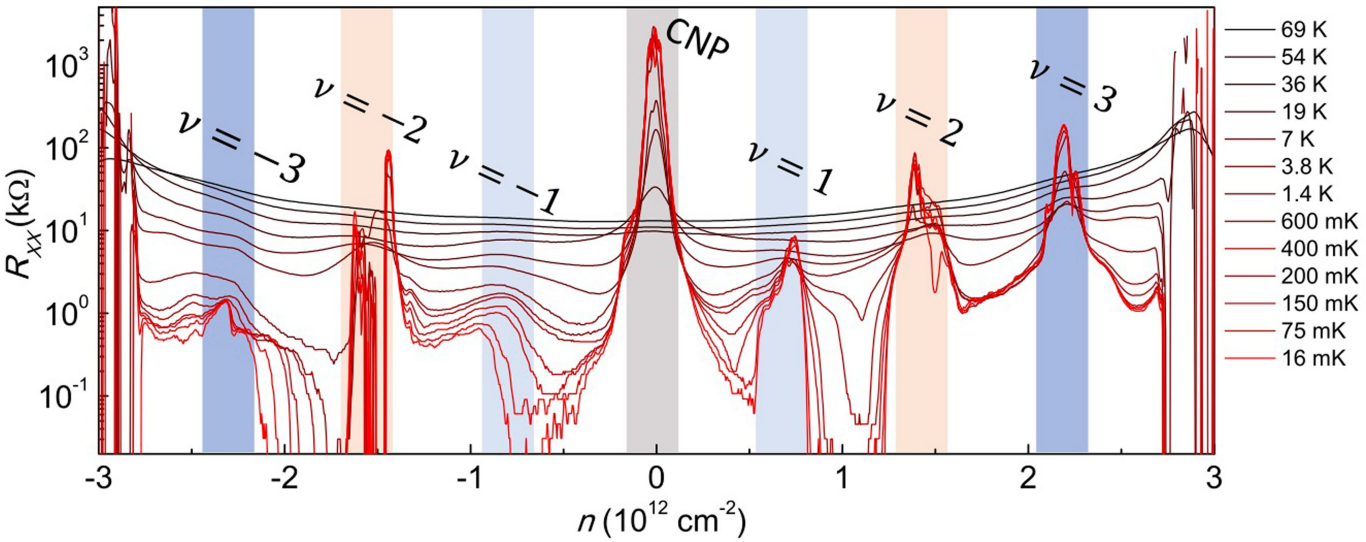

Extended Data Fig. 5 | Four-terminal longitudinal resistance as a function of carrier density at different temperatures. The four-terminal longitudinal resistance is plotted against carrier density n for different temperatures, from 69 K (black trace) to 16 mK (red trace). Coloured vertical bars correspond to the filling factors ν as shown.

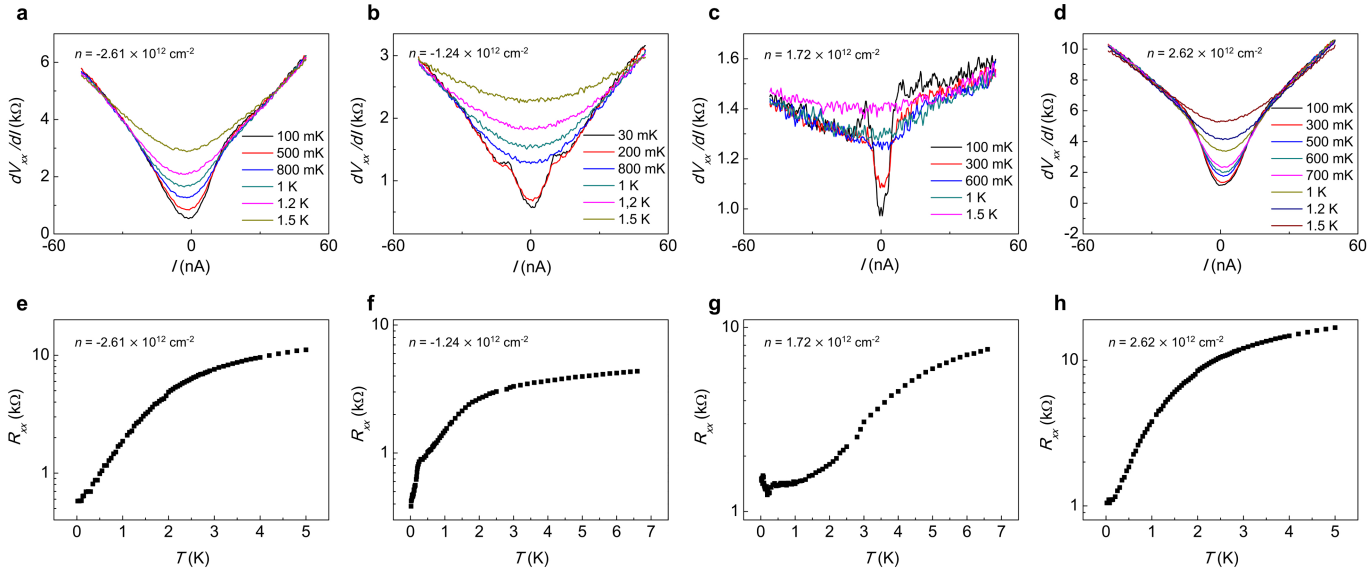

Extended Data Fig. 6 | Additional measurements of other possible superconducting domes. a–d, Differential resistance measurements for additional domes between $-4n_0$ and $-3n_0$ (**a**), $-2n_0$ and $-n_0$ (**b**) $2n_0$ and $3n_0$ (**c**) and $3n_0$ and $4n_0$ (**d**). **e–h**, Corresponding thermal activation measurements of resistance against temperature for the same carrier densities as in **a–d**, respectively.

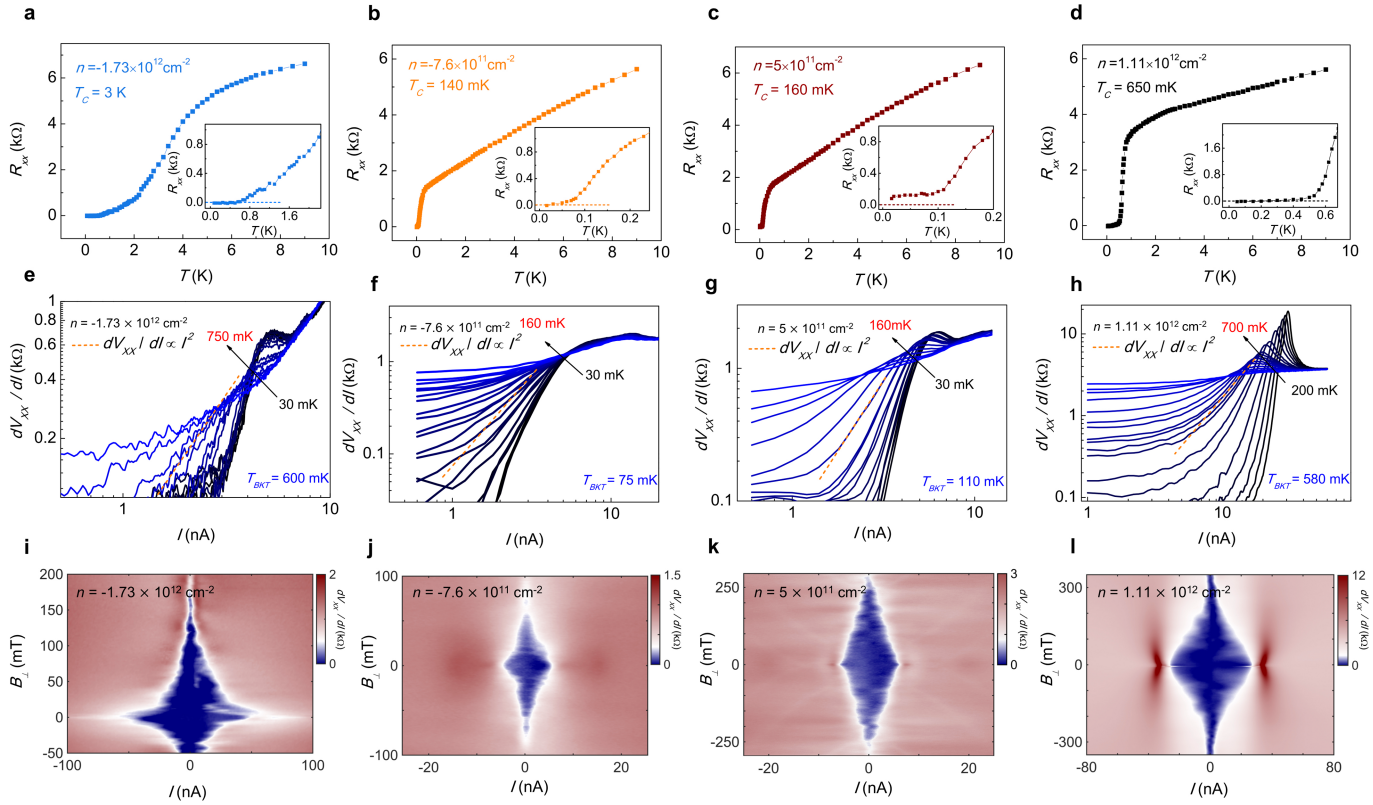

Extended Data Fig. 7 | Full characterization of all four superconducting pockets in sample D1. a–**d**, Thermal activation measurements of resistance against carrier density. The inset shows magnified images, demonstrating that in three superconducting states the resistance drops completely to zero (**a**, **b**, **d**) and in one superconducting state the resistance saturates at about 80 Ω (**c**). **e**–**h**, Differential resistance is plotted against d.c. bias current at various temperatures in order to establish BKT transition temperatures. **i**–**l**, Two-dimensional colour plots of the differential resistance as a function of magnetic field and excitation current at 16 mK.

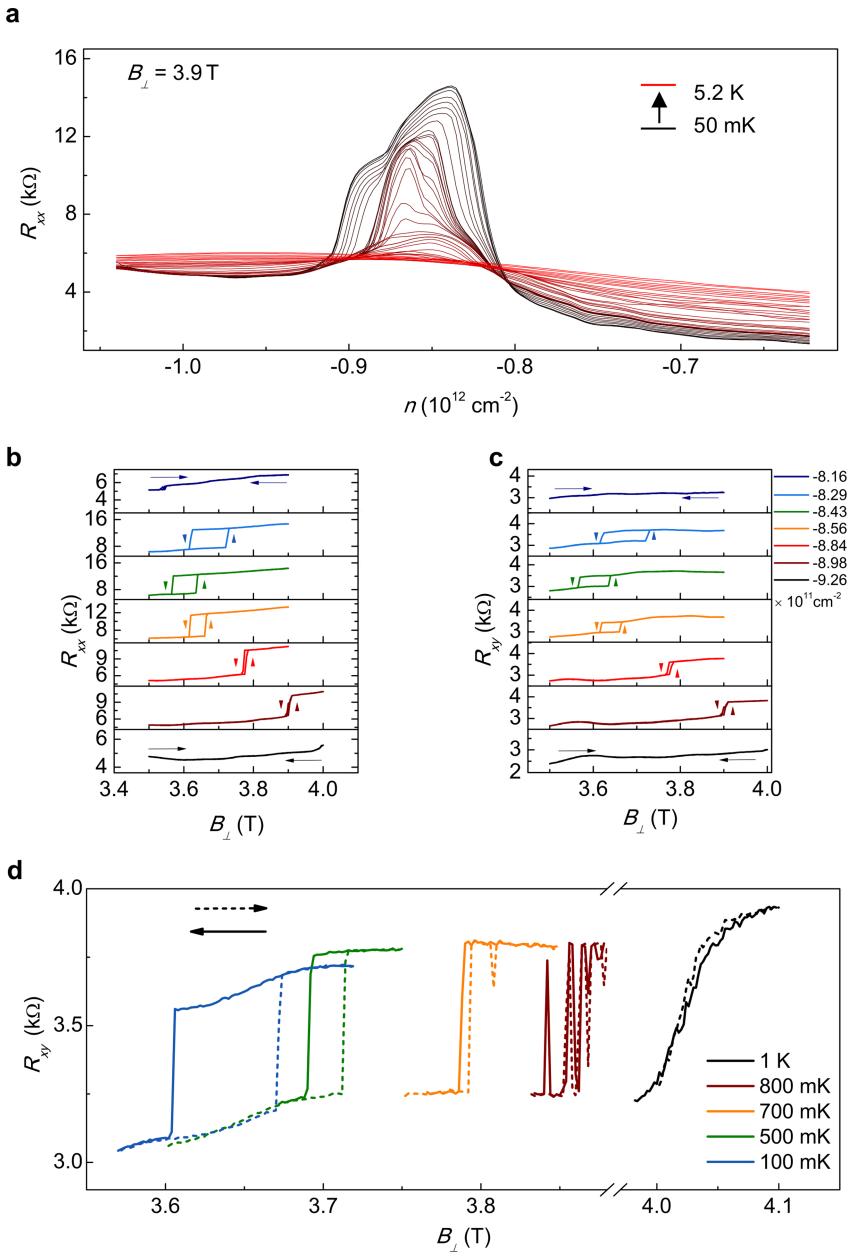

Extended Data Fig. 8 | Additional magnetic hysteresis data. a, Four-terminal longitudinal resistance as a function of carrier density at different temperatures from 50 mK (black trace) to 5.2 K (red trace). **b**, **c**, Plots of longitudinal resistance R_{xx} and transverse resistance R_{xy} against magnetic field at different charge carrier densities and 100 mK. Arrows indicate the sweep direction of the magnetic field. Data from **b** is used to extract data for Fig. 4e. **d**, Transverse resistance plotted against magnetic field at different temperatures (the same dataset as in Fig. 4c). Dashed and solid lines correspond to ascending and descending magnetic fields, respectively.

Extended Data Table 1 | Full dataset for all observed superconducting states in device D1

SC pocket density	T_c (mK)	T_{BKT} (mK)	$B_{C(T=0)}$ (mT)	$\xi_{GL(T=0)}$ (nm)
-1.73×10^{12} cm^{-2}	3000	600	~180	~41
-7.6×10^{11} cm^{-2}	140	75	~100	~55
5×10^{11} cm^{-2}	160	110	~300	~32
1.11×10^{12} cm^{-2}	650	580	~400	~27